Controlling the effective surface mass density of membrane-type acoustic metamaterials using dynamic actuators

Felix Langfeldt[1] and Jordan Cheer[1]

Institute of Sound & Vibration Research, University of Southampton, University Road, Highfield, Southampton, SO17 1BJ, United Kingdom[a)]

Membrane-type acoustic metamaterials (MAM) are thin and lightweight structures that offer exceptional low-frequency sound transmission loss (STL) values, which can exceed the corresponding mass-law significantly. Typically, the high STL of MAM is confined to a narrow frequency band, which is associated with the so-called anti-resonance. This narrow bandwidth reduces the range of potential noise control applications for MAM. To potentially overcome this challenge, this paper presents an investigation into actively controlling the effective surface mass density of MAM by actuating the MAM with a force that is correlated to the acoustic pressure difference acting on the MAM. In particular, it is shown using theoretical and numerical methods that the anti-resonance frequency of MAM can be adjusted over a wide frequency range by passing the incident sound pressure through an adjustable gain. A simple analytical model to predict the frequency shifting, depending on the gain value, is derived. A realization of this concept is further studied, consisting of a circular MAM with a small electrodynamic actuator (to apply a force to the MAM) and a microphone in front of the MAM (to estimate the pressure difference). Finally, experimental results from impedance tube measurements are used to validate the proposed analytical model.

[a]; F.Langfeldt@soton.ac.uk

I. INTRODUCTION

In 2008, Yang *et al.* (2008) proposed membrane-type acoustic metamaterials (MAM) as a new class of locally resonant acoustic metamaterials with properties that are particularly interesting for noise control applications. MAM consist of a periodic arrangement of two-dimensional unit cells which are composed of a thin pre-stressed membrane and added masses attached to the membrane. Even though MAM can be designed to be very thin and lightweight, by carefully tuning the stiffness of the membrane and the added masses, MAM can exhibit anti-resonances at low frequencies with associated sound transmission loss (STL) values that considerably exceed the values expected from a homogeneous plate with the same surface mass density, according to the mass-law (Huang *et al.*, 2016; Naify *et al.*, 2010; Yang *et al.*, 2008). Therefore, MAM provide a promising solution for applications with tonal noise sources and strong constraints on the mass and thickness of acoustic treatments (such as aircraft cabin insulation or mobile sound barriers).

One of the main factors preventing the application of MAM is the narrow bandwidth of the anti-resonances. This means that when either the frequency of the tonal noise source changes (e.g. due to changing rotational speed of aircraft propeller engines) or the properties of the MAM itself change (e.g. due to a reduction in the membrane tension due to an increased temperature), the tonal frequency and the MAM anti-resonance frequency may no longer align and the noise control performance will be significantly decreased.

Numerous studies have aimed to improve the bandwidth of MAM using passive methods. For example, by stacking multiple layers of MAM with different anti-resonance frequencies, a more broadband performance could be achieved (Naify *et al.*, 2012; Yang *et al.*, 2010). This, however, comes at the cost of an increased thickness and overall mass. Other approaches were also proposed using only a single MAM layer with differently tuned neighbouring unit cells (Langfeldt *et al.*, 2018; Naify *et al.*, 2011b; Zhang *et al.*, 2013) or using multiple masses in one unit cell (Lu *et al.*, 2020; Naify *et al.*, 2011a; Zhou *et al.*, 2020). While these approaches do not lead to an increase in the thickness of the MAM, keeping the overall mass unchanged implies that the STL amplitude of the MAM will be reduced as the bandwidth is increased. This has been demonstrated systematically in (Langfeldt and Gleine, 2020) for plate-type acoustic metamaterials, which have acoustical properties that are very similar to MAM. Furthermore, the introduction of additional masses in each unit cell inevitably leads to additional resonances which appear as dips in the STL spectrum with significantly reduced noise reduction. Thus, the unit cells need to be designed carefully to avoid these resonances appearing within the frequency range of interest and no generally applicable method currently exists to perform this design process.

In addition to these purely passive methods, active approaches, that employ actuation mechanisms to adjust the properties of the MAM in-situ and thus its anti-resonance frequency, have also been investigated. In Xiao *et al.* (2015) it was demonstrated that an electric field can be used to modify the resonance frequencies of a MAM unit cell depending on an applied voltage. It was shown experimentally that up to a 25 % reduction in the first MAM resonance frequency was achievable using voltages up to 900 V. A similar approach was followed in (Xiao *et al.*, 2017), where the anti-resonance frequency of a MAM was increased by 16 % using a voltage of 800 V. Instead of electrostatic forces, an actuation based on static pressurization was proposed in Langfeldt *et al.* (2016). In this work, a static pressure difference of 1000 Pa acting on a MAM led to geometric stiffening due to non-linear deformation of the MAM, resulting in an increase in the anti-resonance frequency of about 15 %. Other noteworthy approaches make use of materials which respond to exterior electric or magnetic fields to change the stiffness of the membrane (Chen *et al.*, 2014; Dong *et al.*, 2018).

The aforementioned studies focused only on different actuation mechanisms that could be used to change the acoustic properties of MAM in an open-loop way. However, there have also been several investigations into active acoustic metamaterials using closed-loop strategies. For example, an active acoustic metamaterial with programmable density using piezoelectric diaphragms was investigated in (Akl and Baz, 2012, 2021; Baz, 2010). Other studies also employed piezoelectric diaphragms to develop active acoustic metamaterials that exhibit non-reciprocal transmission of sound (Popa and Cummer, 2014) or can be reconfigured rapidly to change the direction and focal length of scattered waves (Popa *et al.*, 2015). In Tan *et al.* (2022) electrodynamic loudspeakers were combined with a wave-base active noise control in a pipe to realize a non-reciprocal acoustic metamaterial. These studies are noteworthy examples of what could be possible by applying active control algorithms to active MAM—however, meaningful investigations of a truly active MAM have not been published so far, which can be at least partly attributed to the fact that the actuation mechanisms mentioned in the previous paragraph require very high voltages or large additional components (e.g. a compressor to provide pressurized air, as in (Langfeldt *et al.*, 2016)) which made the implementation of practical control systems challenging.

In this paper a new approach to actuating MAM to control their effective density is proposed, with the aim of reducing the complexity of the actuation to allow the exploitation of well-understood control algorithms and to potentially facilitate scaling from a single unit cell to large surfaces with multiple MAM. The concept that is investigated here for the first time is based on using a small electrodynamic actuator, which can be attached to the added mass of the MAM, to impose a dynamic force. It will be shown that by correlating the dynamic force with the incident sound field, the effective density of the MAM can be reconfigured. The configuration of the active MAM studied here consists of the following elements: a circular MAM, a small electrodynamic actuator to apply a dynamic force on the MAM, a microphone in front of the MAM to estimate the pressure difference, and an analogue amplifier with variable gain. The main focus in this paper is on changing the anti-resonance frequency of the MAM, however, this concept can potentially be extended to realise more complex objectives, such as achieving a constant (possibly negative) effective density over a broad bandwidth. The paper is structured as follows: section II provides a numerical study of the effective surface mass density and the sound transmission loss of a MAM actuated by a dynamic force. This study does not include any dynamic properties of the actuation mechanism itself, but serves to provide an understanding of what would theoretically be possible using idealized actuation. In section III it is investigated how the behavior of the proposed active MAM is affected when a small electrodynamic actuator, which can be easily attached to the MAM, is used to provide the actuation force. It will be shown that, within specific frequency limits, a simple analytical model can be used to predict the anti-resonance frequency shifting that can be achieved using the electrodynamic actuator. The results of an experimental implementation of the proposed active MAM inside an impedance tube are presented and discussed in section IV. Finally, a brief summary of the most important results and the conclusions are provided in section V.

II. NUMERICAL ANALYSIS

A. Simulation model

A simulation model based on the finite element method (FEM) has been used to systematically study the effective material properties and sound transmission loss of a MAM with dynamic actuation. A single circular unit cell with a diameter of $D = 84\,\mathrm{mm}$ and a cylindrical mass (diameter: $D_\mathrm{M} = 60\,\mathrm{mm}$, thickness $h_\mathrm{M} = 2\,\mathrm{mm}$) attached to the center of the unit cell was considered, as shown in Figure 1(a). The circular geometry was chosen for the unit cell, because this allows for more efficient numerical modelling (by using an axisymmetric model) and simplifies the test sample design for the measurements in the circular impedance tube, as presented in section IV. The results that will be obtained here for circular MAM unit cells can be readily transferred to rectangular unit cells, as shown by previous research (Langfeldt *et al.*, 2015). In practical applications, MAM will consist of large sheets with a periodic arrangement of such unit cells. It has also been shown previously that the STL of such large-scale multi-celled MAM sheets can be extrapolated from the STL of a single unit cell—even when diffuse incidence and elastic unit cell boundaries are considered (Langfeldt and Gleine, 2019; Zhou *et al.*, 2020). Thus, even though a simplified unit cell geometry will be considered in this work, the results can be transferred to MAM setups that are more relevant in practice.

Because the geometry of the MAM considered here is axisymmetric, a two-dimensional FEM model, as shown in Figure 1(b), was used in the simulations. Figure 1(b) also shows the discretization of the structural model, where second order quadrilateral elements were used for the mass and second order line elements for the membrane. The thickness of the membrane was 55 µm and the in-plane pretension 220 N m^{-1}. The geometry, the materials, and the associated material properties used for the membrane and the mass are provided in Table I. All geometrical and material parameters of the simulation model were chosen to match the experimental test sample, which will be described in section IV. As shown in Figure 1(b), the membrane edge at the perimeter of the MAM was fixed. To represent the dynamic actuation, an out-of-plane point force F was prescribed at the center of the added mass.

B. Effective surface mass density of the actuated MAM

According to Yang *et al.* (2008), the effective surface mass density m''_{eff} of the MAM can be defined, in analogy to Newton's second law of motion, as

$$m''_{\text{eff}} = \frac{\langle \Delta p \rangle}{\langle a_z \rangle} = \frac{\langle \Delta p \rangle}{-\omega^2 \langle w \rangle}, \tag{1}$$

where Δp is the (net) acoustic pressure acting on the MAM, a_z is the acceleration of the MAM in the z direction (normal to the membrane plane), and w is the z component of the displacement. The angular brackets denote an averaging operation over the MAM unit cell

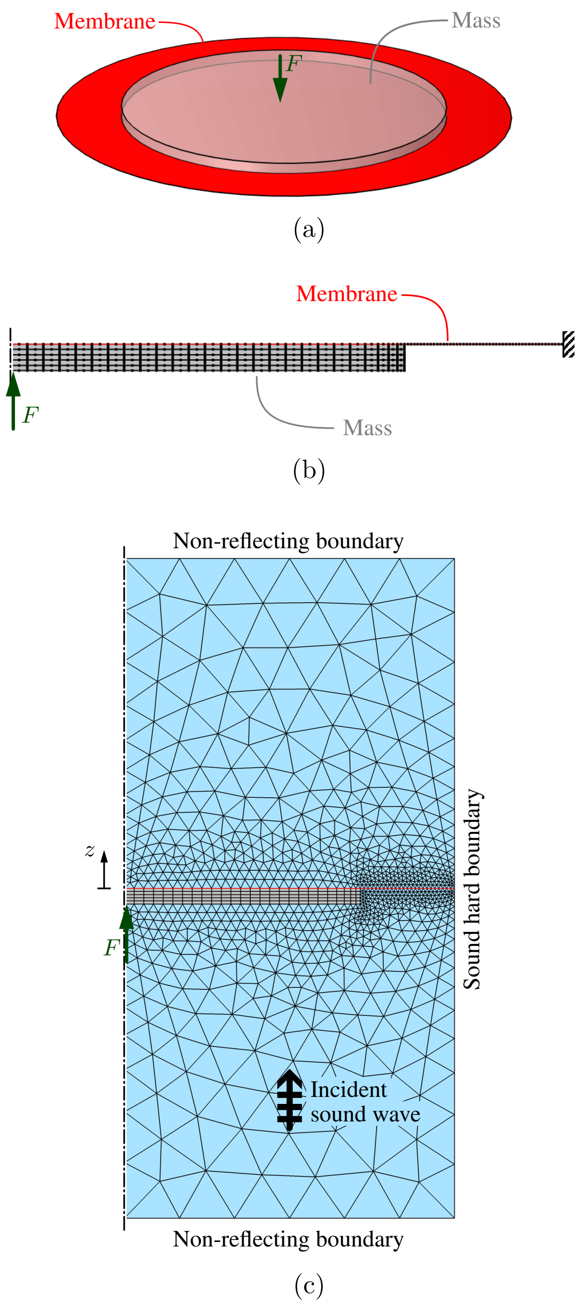

FIG. 1. (Color online) Illustration of the mesh and boundary conditions used in the numerical analysis of the proposed active membrane-type acoustic metamaterial. (a) Isometric view of the unit cell; (b) Axisymmetric structural model, consisting of the membrane and the added mass; (c) Axisymmetric vibro-acoustic model, containing the MAM and surrounding fluid domains.

TABLE I. Material and geometrical parameters used in the simulations.

	Membrane	Mass	
Diameter	84	60	mm
Thickness	0.055	2	mm
Material	PET	Acrylic glass	
Density	1310	1190	$\mathrm{kg\,m^{-3}}$
Young's modulus	2.3	3.2	GPa
Poisson's ratio	0.4	0.35	—
Loss factor	10	5	%

surface S, i.e.

$$\langle w \rangle = \frac{1}{S} \iint\limits_S w \, \mathrm{d}S. \tag{2}$$

In the long wavelength limit the MAM unit cell is much smaller than the acoustic wavelength and the net pressure Δp is approximately uniform across the MAM. Thus, the surface averaged pressure in Equation 1 can be simplified as $\langle \Delta p \rangle = \Delta p$.

When the MAM is excited by both an acoustic pressure field Δp as well as an actuation force F, the resulting displacement field w is given by the superposition of the displacement fields caused by each excitation: $w = w_p + w_F$, which modifies the effective mass equation to give

$$m''_{\text{eff}} = \frac{\Delta p}{-\omega^2 \langle w_p + w_F \rangle} = \frac{\Delta p}{-\omega^2 (\langle w_p \rangle + \langle w_F \rangle)}. \tag{3}$$

Note that $\langle w_p + w_F \rangle = \langle w_p \rangle + \langle w_F \rangle$, because the averaging operation is based on a surface integral (see Equation 2) which can be split into a sum of integrals if the integrand is a sum. The MAM is assumed to be a linear time-invariant system and therefore, the (surface averaged) response of the MAM to both acoustic and force excitation can expressed in terms of the complex poles and zeros of the system as

$$\frac{\langle w_p \rangle}{\Delta p} = K_p \frac{\prod_{i=1}^{\infty} (\mathrm{i}\omega - z_{p,i})\big(\mathrm{i}\omega - z_{p,i}^*\big)}{\prod_{i=1}^{\infty} (\mathrm{i}\omega - p_i)(\mathrm{i}\omega - p_i^*)} \tag{4}$$

and

$$\frac{\langle w_F \rangle}{F} = K_F \frac{\prod_{i=1}^{\infty} (\mathrm{i}\omega - z_{F,i})\big(\mathrm{i}\omega - z_{F,i}^*\big)}{\prod_{i=1}^{\infty} (\mathrm{i}\omega - p_i)(\mathrm{i}\omega - p_i^*)}, \tag{5}$$

where p_i are the complex poles of the MAM, $z_{p,i}$ and $z_{F,i}$ are the complex zeros for pressure and force excitation, respectively, and K_p and K_F are the gains for each excitation. Inserting these zero-pole-gain representations into Equation 3 yields the following expression for the effective surface mass density of the MAM:

$$m''_{\mathrm{eff}} = \frac{\prod_{i=1}^{\infty} (\mathrm{i}\omega - p_i)(\mathrm{i}\omega - p_i^*)}{-\omega^2 K_p \left(\prod_{i=1}^{\infty} (\mathrm{i}\omega - z_{p,i})\big(\mathrm{i}\omega - z_{p,i}^*\big) + \frac{K_F}{K_p} \frac{F}{\Delta p} \prod_{i=1}^{\infty} (\mathrm{i}\omega - z_{F,i})\big(\mathrm{i}\omega - z_{F,i}^*\big) \right)}. \tag{6}$$

This shows that the poles (i.e. the resonances) of the MAM unit cell correspond to the zeros of the effective surface mass density of the MAM. The zeros of the MAM, on the other hand, correspond to the poles of the effective surface mass density, i.e. the frequencies at which the surface averaged displacement is zero and m''_{eff}, by definition, becomes very large. Thus, the roots of the denominator in Equation 6 determine the anti-resonance frequencies of the MAM. By adjusting the ratio $F/\Delta p$—for example using a frequency-independent gain—the anti-resonance frequencies of the MAM can be manipulated by applying a dynamic force F to the MAM.

It should be noted that the poles and zeros used in the equations above are related to the partition impedance of the MAM, which determines the sound transmission properties of an acoustically thin partition. MAM could also be combined with a finite back cavity to realize perfect sound absorbers (Yang *et al.*, 2015) and a pole-zero representation of the MAM similar to Equation 4 could be used to predict the surface impedance and analytically investigate critical coupling. However, the focus of this investigation is on the STL of the MAM, and therefore sound absorption and critical coupling are not further explored.

C. Simplified analytical model

In general, only the low-frequency behaviour of the MAM is of practical interest and the infinite series in Equation 6 can be truncated after a sufficient number of modes. For example, if a symmetric MAM unit cell with a single, rigid added mass is considered, taking into account the first two resonances of the MAM with symmetric mode shapes is usually sufficient (Yang *et al.*, 2014). Additionally, the simulation results for the surface averaged displacement of the numerical MAM model shown in Figure 2(a) and Figure 2(b) indicate that there is one zero within the frequency range of interest for acoustic excitation, but in the case of force excitation no zero appears. Thus, the transfer functions for the surface averaged MAM displacement can be simplified to

$$\frac{\langle w_p \rangle}{\Delta p} \approx \frac{K_p}{4\pi^2} \frac{f_{\mathrm{P}}^2 - f^2}{(f_1^2 - f^2)(f_2^2 - f^2)} \tag{7}$$

and

$$\frac{\langle w_F \rangle}{F} \approx \frac{K_F}{16\pi^4} \frac{1}{(f_1^2 - f^2)(f_2^2 - f^2)}, \tag{8}$$

where f_1 and f_2 are the first two resonance frequencies and f_P is the MAM anti-resonance frequency. It should be noted that, for the sake of simplicity of this analysis, no damping is considered here so that the complex poles and zeros of the MAM are purely imaginary. Expressions for the modal quantities in Equation 7 and Equation 8 have been determined using the numerical model and are provided in Table II. The comparison of the direct frequency response results from the FEM model and the simplified expressions in Equation 7 and Equation 8 is shown in Figure 2(a) and Figure 2(b). These plots demonstrate that the expressions provide an excellent representation of the surface averaged response of the MAM for both acoustic and point force excitation over this frequency range. Note that $f_2 = 1679\,\mathrm{Hz}$ is considerably larger than the highest frequency of interest ($1000\,\mathrm{Hz}$), but it was included in the analytical computations using Equation 7 and Equation 8 to improve the accuracy of the model around $1000\,\mathrm{Hz}$. As a general rule of thumb, which is often applied in modal truncations of numerical simulation models, all poles with eigenfrequencies up to twice the maximum frequency of interest should be included in the modal expansion of the MAM.

Inserting the truncated series representation into Equation 6 yields the following simplified expression for the effective surface mass density of a MAM with both acoustic and point force excitation:

$$m''_\mathrm{eff} = -\frac{1}{f^2} \frac{(f_1^2 - f^2)(f_2^2 - f^2)}{K_p(f_\mathrm{P}^2 - f^2) + \frac{1}{4\pi^2} K_F \frac{F}{\Delta p}}. \tag{9}$$

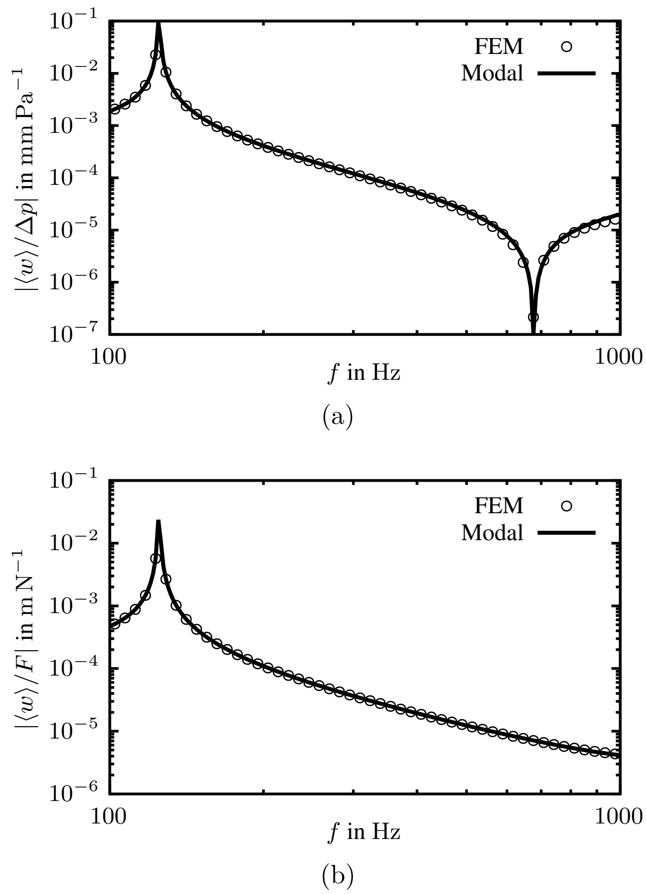

FIG. 2. Magnitude of the surface averaged displacement of the MAM. Symbols represent the numerical results from the FEM model, the curves have been obtained using the simplified models Equation 7 and Equation 8 with the modal parameters given in Table II. (a) Acoustic excitation; (b) Point force excitation.

If the force F is assumed to be driven by a proportional controller with a frequency-independent gain G and Δp being the input signal, the effective surface mass density of the MAM becomes

$$m''_{\text{eff}} = -\frac{1}{f^2} \frac{(f_1^2 - f^2)(f_2^2 - f^2)}{K_p \left(\tilde{f}_{\text{P}}^2 - f^2 \right)}. \tag{10}$$

TABLE II. Modal parameters of the MAM used in Equation 9. These values have been obtained using the numerical model of the MAM.

f_1	f_2	f_P	K_p	K_F
125	1679	677	2.63	1.16×10^{10}
Hz	Hz	Hz	$\mathrm{m^2\,kg^{-1}}$	$\mathrm{kg^{-1}\,s^{-2}}$

This equation has the exact same form as the effective surface mass density of a MAM with purely acoustic excitation, however with a modified anti-resonance frequency $\tilde{f}_\mathrm{P}$, given by

$$\tilde{f}_\mathrm{P} = \sqrt{f_\mathrm{P}^2 + \frac{K_F}{4\pi^2 K_p} G}. \tag{11}$$

This modified anti-resonance frequency can be reduced using a negative gain G and increased by using a positive gain G. In the case of $G = 0$, no force is exerted on the MAM and the original anti-resonance frequency f_P is retained.

D. Sound transmission loss

The active control of the effective surface mass density of the MAM has been studied in the previous sub-section using a known pressure loading Δp. In the practical case of sound being transmitted through the MAM, the pressure loading Δp is governed by the incident, reflected, and transmitted sound fields. As shown in section II C, the acoustic loading needs to be known to be able to control the MAM anti-resonance frequencies, but a lot of effort would be required in practice to measure Δp in full detail. Therefore, replacing Δp with quantities that are much simpler to measure or estimate would be beneficial.

Since the MAM is acoustically thin, Δp can be expressed as

$$\Delta p \approx p_{\mathrm{bl}} - 2\hat{p}_{\mathrm{t}}, \tag{12}$$

where p_{bl} is the blocked pressure field, corresponding to the acoustic pressure on the MAM if it were a perfectly reflecting boundary, and $\hat{p}_{\mathrm{t}}$ is the amplitude of the transmitted sound wave. This can be further simplified by noting that the anti-resonance frequency of the MAM is of primary interest in this work. Since the STL of the MAM is very high around this frequency, the amplitude of the transmitted sound wave is much smaller than the incident sound wave. Thus, Equation 12 can be further simplified to provide an estimate for the pressure difference Δp based only on the blocked pressure field: $\Delta p \approx p_{\mathrm{bl}}$. In practice, the blocked pressure p_{bl} could be determined by measuring the incident sound field generated by the noise source and using a filter to predict p_{bl} based on a reference signal applied to the noise source. A more direct way would be to use a small microphone (e.g. a MEMS microphone) located on top of the MAM to measure the pressure p_1 on the upper MAM surface and use this as an estimate of the blocked pressure: $\Delta p \approx p_{\mathrm{bl}} \approx p_1$.

The FEM model described in section II A has been extended by fluid domains on top and below the MAM (see Figure 1(c)). These fluid domains were truncated with non-reflecting boundary conditions to minimize the reflection of plane acoustic waves. The lateral boundary conditions were prescribed as axisymmetric (on-axis) and sound hard (at the MAM unit cell edge location). The MAM was acoustically excited by a plane acoustic wave travelling in the positive z-direction defined as

$$p_{\mathrm{i}}(z) = \hat{p}_{\mathrm{i}} \exp(-\mathrm{i}k_0 z), \tag{13}$$

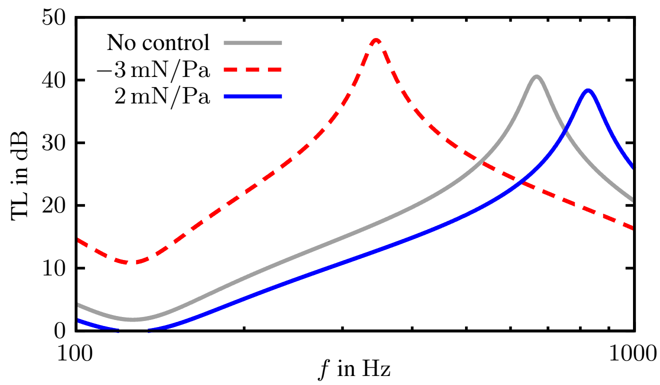

FIG. 3. (Color online) Simulated sound transmission loss of the MAM at different gain values G.

where $\hat{p}_\mathrm{i}$ is the incident wave amplitude at $z = 0$ (i.e. the MAM surface) and k_0 is the wave number of the fluid. The acoustic pressure p_1, which was used for the active control of the MAM, was extracted using a point probe located at the center of the added mass (corresponding to the actuation force point indicated in Figure 1(c)). The discretization of the MAM was the same as in the structural model (see Figure 1(b)). For the fluid, second order triangular elements have been used which were coupled to the structural model using two-way vibro-acoustic coupling. The density and speed of sound of the fluid were given by $\rho_0 = 1.2\,\mathrm{kg\,m^{-3}}$ and $c_0 = 343\,\mathrm{m\,s^{-1}}$, respectively. The transmission loss TL of the MAM was determined by integrating the transmitted sound intensity over the outlet boundary to obtain the transmitted sound power W_t. The transmission loss is then given by

$$\mathrm{TL} = -10\,\mathrm{lg}\left(\frac{W_\mathrm{t}}{W_\mathrm{i}}\right), \tag{14}$$

where $W_\mathrm{i} = 0.25\pi D^2 |\hat{p}_\mathrm{i}|^2/(2\rho_0 c_0)$ is the incident sound power.

The simulation results for two different gain values are shown in Figure 3. A negative gain of $G = -3\,\mathrm{mN\,Pa^{-1}}$ leads to a reduction of the anti-resonance frequency of the MAM to about 345 Hz. Using a positive gain of $2\,\mathrm{mN\,Pa^{-1}}$, on the other hand, shifts the MAM anti-

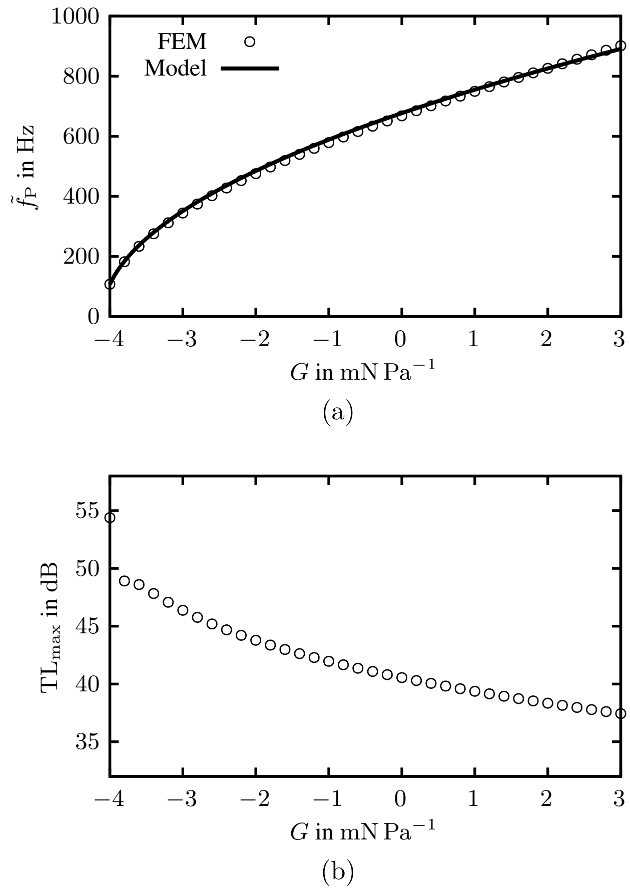

FIG. 4. (Color online) Effect of the gain G on the MAM anti-resonance properties. (a) Shifted anti-resonance frequency $\tilde{f}_P$ and comparison with Equation 11; (b) Maximum STL value at $\tilde{f}_P$.

resonance frequency to higher frequencies. In Figure 4(a) it is shown how the anti-resonance frequency of the active MAM $\tilde{f}_P$ changes for different values of G, comparing the simulation results to the prediction from the analytical model in Equation 11. The agreement with Equation 11 is very good, which confirms that this model can be used to predict the anti-resonance frequency $\tilde{f}_P$ in a sound transmission configuration. Additionally, Figure 4(b) shows the change in the maximum STL value at the shifted MAM anti-resonance $\mathrm{TL_{max}}$. Qualitatively, the $\mathrm{TL_{max}}$ values slightly decrease as G is increased. This is in line with the results shown in Figure 3, where increasing the gain generally leads to a moderate decrease of the STL values.

III. ACTUATION WITH ELECTRODYNAMIC ACTUATOR

A. Analytical model of the actuator force

In practice, the force F that is applied to the MAM is generated by an actuator that is mechanically coupled with the MAM. Depending on the type of actuator, an input signal U is filtered by the dynamical behaviour of the actuator and the resulting force F is related to the input signal via a frequency response function H_F. Thus, it is likely that the anti-resonance frequency shifting behaviour of the active MAM will be altered by the actuator dynamics.

In this study, a small electrodynamic actuator (mass M_{act}) attached to the top of the mass was used due to its wide commercial availability and low-cost. The force F exerted on the MAM by the actuator can be expressed as follows (see Rohlfing *et al.* (2011) for derivations):

$$F = \mathrm{i}\omega Z_{\mathrm{b}} w_{\mathrm{b}} + H_{\mathrm{b}} U, \tag{15}$$

where

$$Z_{\mathrm{b}} = Z_{M_{\mathrm{b}}} + \frac{Z_{M_{\mathrm{ms}}}\left(Z_{\mathrm{s}} + \frac{B\ell^2}{Z_{\mathrm{e}}}\right)}{Z_{M_{\mathrm{ms}}} + Z_{\mathrm{s}} + \frac{B\ell^2}{Z_{\mathrm{e}}}} \tag{16}$$

is the passive base impedance of the actuator and

$$H_{\mathrm{b}} = \frac{B\ell}{Z_{\mathrm{e}}} \frac{Z_{M_{\mathrm{ms}}}}{Z_{M_{\mathrm{ms}}} + Z_{\mathrm{s}} + \frac{B\ell^2}{Z_{\mathrm{e}}}} \tag{17}$$

is the blocked force response of the actuator due to the applied voltage U. In Equation 16 and Equation 17, $Z_{M_\mathrm{b}} = \mathrm{i}\omega M_\mathrm{b}$ and $Z_{M_\mathrm{ms}} = \mathrm{i}\omega M_\mathrm{ms}$ are the impedances of the base mass ($M_\mathrm{b} = M_\mathrm{act} - M_\mathrm{ms}$) and moving mass ($M_\mathrm{ms}$) of the actuator, respectively, $Z_\mathrm{s} = D_\mathrm{ms} + 1/(\mathrm{i}\omega C_\mathrm{ms})$ is the mechanical impedance of the suspension, and $Z_\mathrm{e} = R_\mathrm{e} + \mathrm{i}\omega L_\mathrm{e}$ is the electrical impedance of the electrical circuit within the actuator. $B\ell$ is the force factor of the actuator. The compliance of the suspension, C_ms, is related to the resonance frequency of the actuator via $C_\mathrm{ms} = 1/(M_\mathrm{ms}(2\pi f_\mathrm{ms})^2)$ and the damping constant D_ms can be obtained using $D_\mathrm{ms} = 2\zeta_\mathrm{ms}\sqrt{M_\mathrm{ms}/C_\mathrm{ms}}$, where ζ_ms is the damping ratio of the suspension.

In principle, Equation 15 could be used, for example in Equation 9, to obtain the effective surface mass density of the MAM with a voltage U applied to the actuator. However, due to the passive mechanical impedance Z_b, this requires additional information about the frequency-dependent displacement amplitude of the MAM at the actuator base location. In order to obtain a simple expression for an estimate of the anti-resonance frequency shifting possible with an electrodynamic actuator, Equation 15 is simplified under the following two assumptions: (1) The part of the actuator force related to the passive mechanical impedance Z_b is much smaller than the blocked force: $\mathrm{i}\omega Z_\mathrm{b} w_\mathrm{b} \ll H_\mathrm{b} U$. This assumption is reasonable for frequencies sufficiently far away from the resonances of the MAM and actuator, where displacements are typically small. (2) The blocked force is proportional to the input voltage U: $H_\mathrm{b} \approx B\ell/R_\mathrm{e}$. This is a good approximation for frequencies that are larger than f_ms and smaller than the cut-off frequency of the RL filter $f_\mathrm{c} = R_\mathrm{e}/(2\pi L_\mathrm{e})$. Thus, the simplified expression for the actuator force is given by

$$F \approx \frac{B\ell}{R_\mathrm{e}} U. \tag{18}$$

Consequently, the gain G, which was used so far to represent the ratio of the force applied to the MAM and the acoustic pressure difference, can be expressed as

$$G = \frac{F}{\Delta p} \approx \frac{B\ell}{R_\mathrm{e}} \frac{U}{\Delta p} = \frac{B\ell}{R_\mathrm{e}} G_U, \tag{19}$$

with G_U being the electrical gain (units: $\mathrm{V\,Pa^{-1}}$). By inserting Equation 19 into Equation 11, the expression

$$\tilde{f}_\mathrm{P} = \sqrt{f_\mathrm{P}^2 + \frac{K_F}{4\pi^2 K_p} \frac{B\ell}{R_\mathrm{e}} G_U} \tag{20}$$

can be obtained which shows that, within the validity range of the aforementioned assumptions, the anti-resonance frequency shifting with the actuator is the same as for the idealized case with an excitation using a known point force F. The only difference is that the gain is altered by the factor $B\ell/R_\mathrm{e}$.

B. Numerical simulations

To investigate the properties of the active MAM actuated using an electrodynamic actuator and compare the anti-resonance frequency shifting with the simplified model in Equation 20, the FEM simulation model of the MAM has been extended to include the actuator. This was done by representing the actuator as a lumped electro-mechanical model, as shown in Figure 5, and coupling this model with the FEM model of the MAM by enforcing the base displacement w_b and the actuator force F to be continuous at the actuator attachment point in the center of the added mass of the MAM. The mechanical and electrical parameters used in the model of the actuator are provided in Table III. These values correspond to the

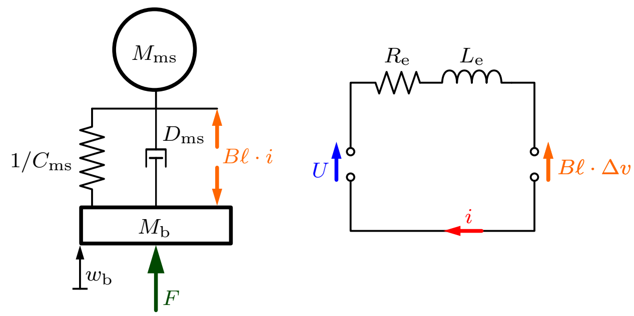

FIG. 5. (Color online) Lumped electro-mechanical representation of the electrodynamic actuator used in the simulation model.

TABLE III. Mechanical and electrical parameters of the electrodynamic actuator used in the numerical and experimental studies.

M_{act}	M_{ms}	f_{ms}	ζ_{ms}	L_{e}	R_{e}	$B\ell$
3.33 g	3.2 g	180 Hz	6.3 %	0.17 mH	8.8 Ω	1.01 T m

actuator used in the experiments (Tectonic type TEAX09C005-8) and the properties of this type of actuator have been studied systematically by Singleton *et al.* (2022).

Figure 6(a) shows the simulated sound transmission loss for different values of the electrical gain G_U. The dashed grey curve indicates the STL of the MAM without the actuator, while the solid grey curve corresponds to the MAM with the actuator and $G_U = 0$. By comparing these curves, it can be seen that the original anti-resonance frequency of the MAM at $f_{\mathrm{P}} = 677\,\mathrm{Hz}$ is almost unchanged when the actuator is added. This can be explained by the moving mass of the actuator M_{ms} amounting to over 96 % of the actuator mass and at frequencies well above the resonance frequency of the actuator ($f_{\mathrm{ms}} = 180\,\mathrm{Hz}$), the moving

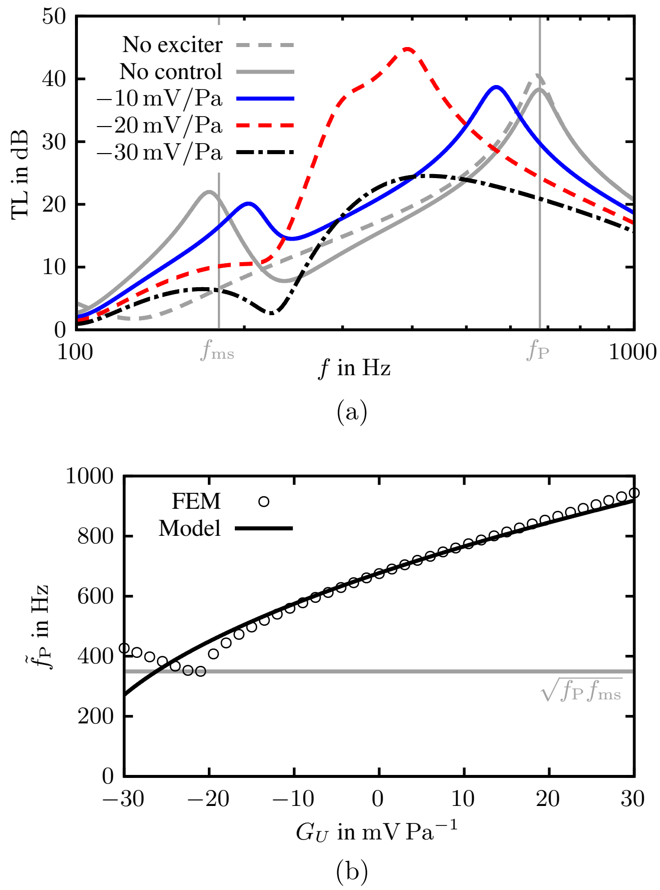

FIG. 6. (Color online) Simulation results for the effect of the electrical gain G_U on the vibro-acoustic properties of the active MAM with an electrodynamic actuator. (a) Sound transmission loss for different values of G_U; (b) Shifted anti-resonance frequency $\tilde{f}_{\mathrm{P}}$ and comparison with Equation 20.

mass becomes effectively decoupled from the actuator base and therefore does not affect the inertial properties of the MAM at f_{P}. Only a small reduction of the peak STL values can be seen due to the losses in the mechanical suspension and the electrical circuit of the actuator.

At lower frequencies, the impact of the actuator on the passive MAM is much stronger. The actuator resonance is visible as a strongly damped additional peak slightly below f_{ms}. This indicates that in this frequency range the passive base impedance of the actuator Z_{b} cannot be neglected due to the resonant behavior of the actuator.

The curves in Figure 6(a) for non-zero values of G_U demonstrate that the anti-resonance frequency can be reduced by using negative values of G_U, similar to the previous results obtained for a direct application of an actuation force F. However, it can also be seen that—in this simple control setup—the peak at the actuator resonance shifts in the opposite direction and approaches the shifted MAM anti-resonance as G_U becomes increasingly negative. For $G_U = -10\,\mathrm{mV\,Pa^{-1}}$, the two peaks can still be separated quite well. At $-20\,\mathrm{mV\,Pa^{-1}}$, both peaks almost merge into a single peak roughly around the geometric mean of f_{ms} and f_{P}, forming a relatively broad frequency range with much higher STL values than the passive MAM. A further decrease of G_U to $-30\,\mathrm{mV\,Pa^{-1}}$ leads to a significant reduction in the STL at this merged peak and the overall sound insulation performance of the active MAM. This indicates that when the anti-resonance frequency of the MAM is shifted close to the frequency range where the mechanical behavior of the actuator is governed by its resonance, the actuator force cannot be considered to be proportional to the input voltage U any more (as in Equation 18) and the behavior of the active MAM deviates from the idealized case with a direct application of an actuation force F.

The results shown in Figure 6(b) confirm this over a wide range of values for G_U and also show how the anti-resonance frequency can be shifted up in frequency with a postive value for G_U. As long as the value of G_U is well above $-15\,\mathrm{mV\,Pa^{-1}}$, the shifted anti-resonance frequencies $\tilde{f}_{\mathrm{P}}$ follow the curve predicted by the simplified model given in Equation 20 quite well. However, as $\tilde{f}_{\mathrm{P}}$ approaches a limiting frequency at $\sqrt{f_{\mathrm{P}} f_{\mathrm{ms}}} = 360\,\mathrm{Hz}$, the simulated values start to deviate from Equation 20 and do not become smaller than the limiting frequency, even for gain values below $-20\,\mathrm{mV\,Pa^{-1}}$. In summary, the simulation results show that an electrodynamic actuator can be used with a simple proportional controller to change the anti-resonance frequencies of MAM in accordance with Equation 20, as long as $\tilde{f}_{\mathrm{P}} > \sqrt{f_{\mathrm{P}} f_{\mathrm{ms}}}$.

IV. EXPERIMENTAL STUDY

A. Test sample and measurement method

Impedance tube measurements were performed according to ASTM E2611–09 (four microphone method) to demonstrate the working principle of the proposed active MAM unit cell. The test sample that was built for the experiments is shown in Figure 7(a). A PET film was glued on a 3D printed ring shaped sample holder (outer diameter: 100 mm; inner diameter: 84 mm) and the membrane pretension was applied by shrinking the film using a heat gun. The nominal material parameters and thickness of the PET film correspond to the values used in the simulation study. The pretension of $220\,\mathrm{N\,m^{-1}}$, which was used in the FEM model, was determined by acoustically measuring the first resonance frequency of the membrane (without added mass) and fitting the pretension in the FEM model to match this frequency. An acrylic glass disc was then glued onto the membrane using cyanoacrylate glue to ensure a good mechanical coupling between the membrane and the mass. Then, the type TEAX09C005-8 actuator was attached to the center of the mass using the adhesive strips provided with the actuator.

A schematic representation of the impedance tube setup is shown in Figure 7(b). According to ASTM E2611–09, four microphones were used (two on each side of the MAM) in

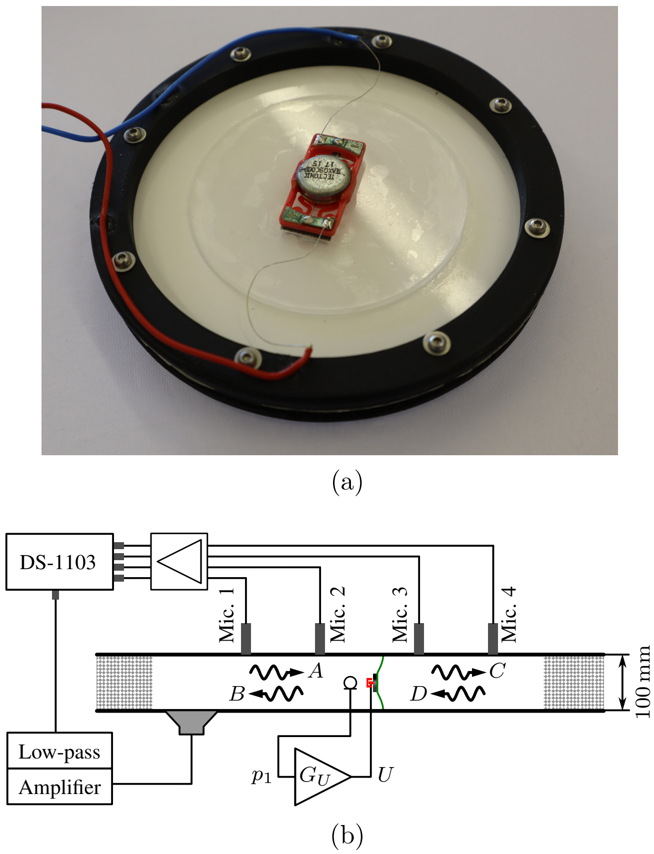

FIG. 7. (Color online) Impedance tube measurement setup used for the experimental study. (a) Test sample of the active MAM unit cell; (b) Schematic representation of the measurement method.

order to determine the amplitudes A, B, C, and D of the plane waves propagating inside the tube. Both ends of the tube were terminated using sound absorbing material to minimize reflections and a loudspeaker was used on one side of the MAM to excite the sound field. A dSPACE DS-1103 data acquisition system was used for the generation of the signal supplied to the loudspeaker and the acquisition of the four impedance tube microphone signals. The sampling frequency was 4 kHz and in each measurement the signals were recorded for 30 s to ensure sufficient averaging. A random noise signal was provided to the loudspeaker during all acoustic measurements. The signal provided to the actuator was dependent on the specific measurement situation and will be described in more detail in the following subsections.

B. System identification

To first evaluate the accuracy of the FEM model used in this investigation, the primary and secondary path responses have been measured. For this purpose, two different measurements were performed:

1. Primary path response (random noise excitation of the loudspeaker)

2. Secondary path (or plant) response (random noise excitation of the actuator)

In the first measurement, the acoustic transmission factor $t = \hat{p}_\mathrm{t}/\hat{p}_\mathrm{i}$ and reflection factor $r = \hat{p}_\mathrm{r}/\hat{p}_\mathrm{i}$ of the passive MAM were determined as per ASTM E2611–09. The transmitted pressure $\hat{p}_\mathrm{t}$ due to the excitation of the actuator in the second measurement was determined via $\hat{p}_\mathrm{t} = C - A \cdot t - D \cdot r$, in order to correct for sound waves being reflected at the terminations of the impedance tube.

Figure 8(a) and Figure 8(b) show a comparison of the magnitude and phase, respectively, of the acoustic transmission factor $\hat{p}_\mathrm{t}/\hat{p}_\mathrm{i}$. Overall, the agreement between the simulations and the experimental measurements is very good. In the magnitude plot in Figure 8(a) it can be seen that the shape of the anti-resonance (the dip at 677 Hz) is captured quite well by the numerical model. The anti-resonance frequency is slightly lower than in the measurements, which could be attributed to slight deviations in the manufactured sample from the specified nominal material or geometrical parameters and the membrane pretension.

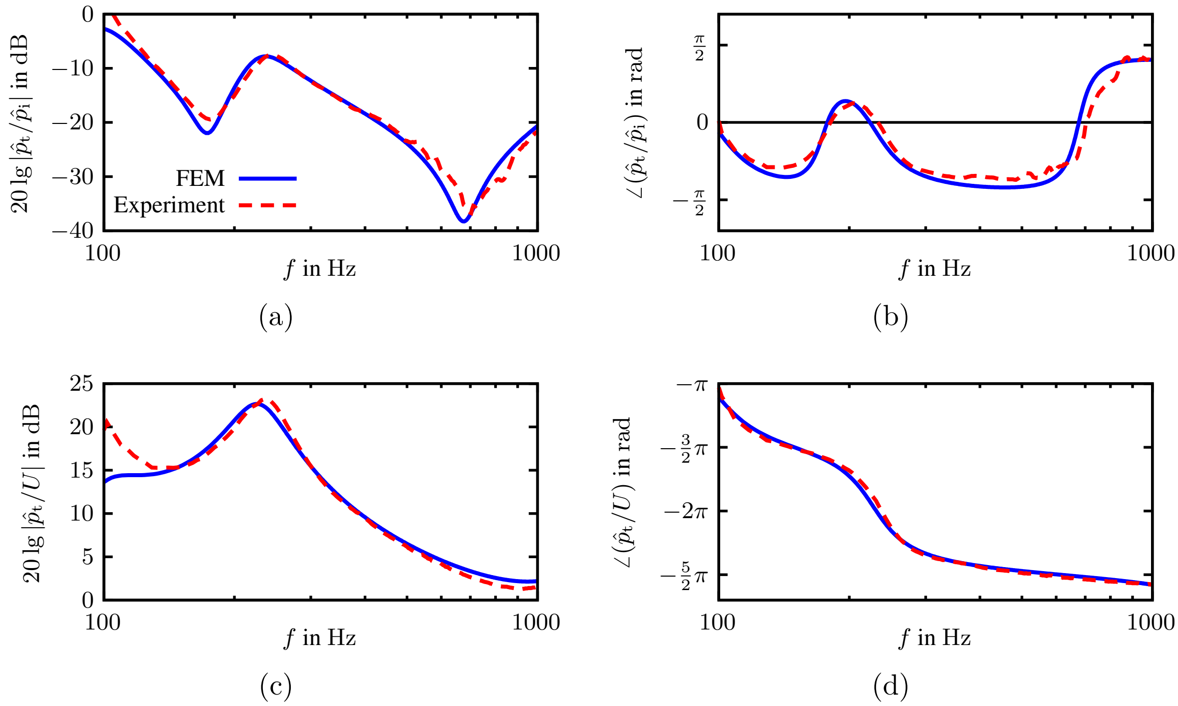

FIG. 8. (Color online) Measured and simulated primary and secondary path responses of the active MAM test sample. (a) Magnitude and (b) phase of the transmitted acoustic pressure for acoustic excitation (primary path); (c) Magnitude and (d) phase of the transmitted acoustic pressure for electrical excitation (secondary path).

Also, the additional peak and dip caused by the actuator below 300 Hz are well represented by the FEM model. Only at very low frequencies more significant deviations occur, but these can be accepted, because the analysis focuses mainly on frequencies well above 100 Hz. The phase in Figure 8(b) also shows a very good agreement over most frequencies.

The magnitude of the transmitted pressure $\hat{p}_t$ for a given actuator voltage U is plotted in Figure 8(c). A good agreement between simulations and measurements can be observed, giving confidence in the modelling of the actuator and its coupling to the MAM. As in the primary path response, the deviations between simulation and experiment at very low frequencies can be accepted. Finally, the phase of the electrical excitation transfer function is shown in Figure 8(d), indicating that the simulation model of the actuator also provides a very good estimation of the phase response.

C. Anti-resonance frequency shifting

Next, to measure the anti-resonance frequency shifting of the active MAM, a microphone was placed in front of the MAM to measure p_1, as shown in Figure 7(b). The microphone signal was amplified using an analogue voltage amplifier with an adjustable gain G_U. This amplified signal U was then fed into the actuator. The measurements were performed for several gain values G_U between -30 and $30\,\mathrm{mV\,Pa^{-1}}$. Figure 9(a) shows, as an example, the measured and simulated transmission loss for $G_U = 23.1\,\mathrm{mV\,Pa^{-1}}$. In general, the change in the anti-resonance frequency and the associated STL values observed in the experimental results are very similar to what the FEM model predicts. To compare measurements and simulations over a wider range of gain values, Figure 9(b) shows the shifted anti-resonance frequency $\tilde{f}_\mathrm{P}$ for different values of G_U. The experimentally determined anti-resonance frequencies match the trend from the simulations and the prediction from Equation 20 quite well. For $G_U > -20\,\mathrm{mV\,Pa^{-1}}$, the experimentally determined values of $\tilde{f}_\mathrm{P}$ are systematically higher than in the simulations and the analytical model. This general trend can be explained by the slight underprediction of the passive MAM anti-resonance frequency in the model (as explained in section IV B), which results in an underprediction of the shifted anti-resonance frequencies $\tilde{f}_\mathrm{P}$ as well. This systematic error could be reduced by tuning the FEM model, e.g. by slightly increasing the membrane tension.

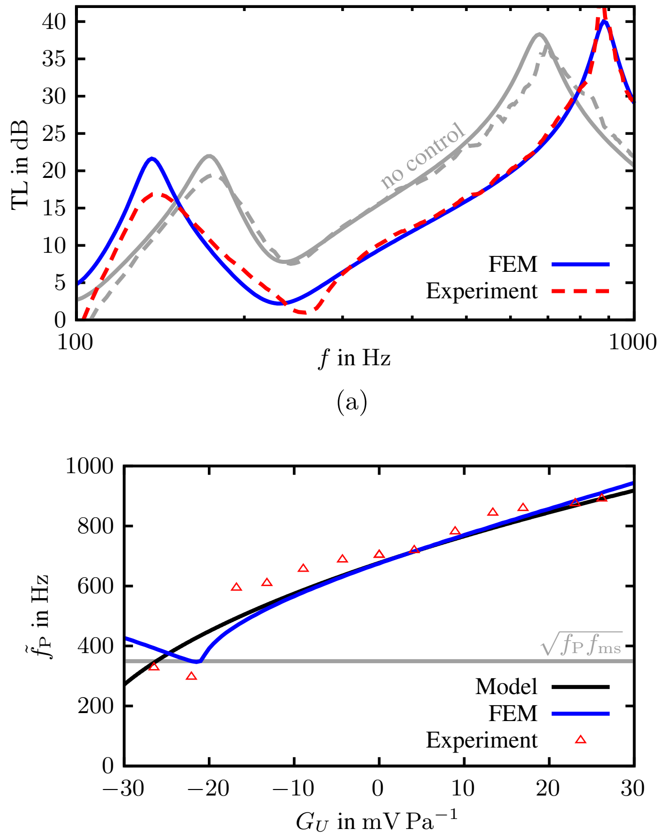

(b)

FIG. 9. (Color online) Comparison of measurements and simulation results for the effect of the electrical gain G_U on the vibro-acoustic properties of the active MAM with an electrodynamic actuator. (a) Sound transmission loss at $G_U = 23.1\,\mathrm{mV\,Pa^{-1}}$; (b) Anti-resonance frequency shifting.

V. CONCLUSIONS

In this contribution, the reconfiguration of the effective surface mass density of a membrane-type acoustic metamaterial (MAM) using a dynamic actuator has been investigated using analytical, numerical, and experimental methods. The proposed active MAM uses the actuator to exert a dynamic force on the MAM which can be exploited to actively change the effective properties of the metamaterial. Using an idealized model it could be shown that by correlating the actuator force with the acoustic pressure difference on the MAM, the effective surface mass density of the MAM can be altered. In particular, a proportional controller with a variable gain can be used to adapt the anti-resonance frequencies of the active MAM. A simple equation for predicting the shifted anti-resonance frequency depending on the proportional gain has been derived. In the next step, it was investigated how the properties of the active MAM are affected when the actuation force is provided by an electrodynamic inertial actuator. Using simulations it could be demonstrated that above a certain limiting frequency, corresponding to the geometric mean of the mechanical resonance frequency of the actuator and the passive MAM anti-resonance frequency, the anti-resonance frequency shifting can be predicted using the same equation as for the idealized case. Finally, an experimental test sample of the proposed active MAM has been build up and its functionality was demonstrated using impedance tube measurements.

The proposed active MAM offers several advantages over previously investigated reconfigurable MAM designs: Firstly, the anti-resonance frequency could be shifted over a much larger range (over one octave in the experiments) using much lower voltages than before. Secondly, the actuation can be applied using a small actuator which allows for a compact and flexible integration, retaining the low thickness and lightweight properties which make MAM so attractive for different noise control applications. Finally, the control algorithm using a proportional gain investigated here is the simplest possible implementation. The dynamic character of the actuators enables much more complex control algorithms, e.g. using inverse filters to generate a flat blocked force over a much wider frequency range enabling even larger anti-resonance frequency shifts, or using adaptive filters, which could be investigated in the future to further enhance the noise insulation properties of MAM and making them more applicable to noise control problems.

ACKNOWLEDGMENTS

F. Langfeldt's research was funded by the Deutsche Forschungsgemeinschaft (DFG, German Research Foundation) in the framework of the Walter Benjamin Programme (grant no. 455631459). The authors acknowledge the use of the IRIDIS High Performance Computing Facility, and associated support services at the University of Southampton, in the completion of this work.

Akl, W., and Baz, A. (**2012**). "Analysis and experimental demonstration of an active acoustic metamaterial cell," Journal of Applied Physics **111**(4), 044505, doi: 10.1063/1.3686210.

Akl, W., and Baz, A. (**2021**). "Active control of the dynamic density of acoustic metamaterials," Applied Acoustics **178**, 108001, doi: 10.1016/j.apacoust.2021.108001.

Baz, A. (**2010**). "An Active Acoustic Metamaterial With Tunable Effective Density," Journal of Vibration and Acoustics **132**, doi: 10.1115/1.4000983.

Chen, X., Xu, X., Ai, S., Chen, H., Pei, Y., and Zhou, X. (**2014**). "Active acoustic metamaterials with tunable effective mass density by gradient magnetic fields," Applied Physics Letters **105**(7), 071913, doi: 10.1063/1.4893921.

Dong, L., Grissom, M. D., Safwat, T., Prasad, M. G., and Fisher, F. T. (**2018**). "Resonant frequency tuning of electroactive polymer membranes via an applied bias voltage," Smart Materials and Structures **27**(11), 114005, doi: 10.1088/1361-665X/aacdc0.

Huang, T.-Y., Shen, C., and Jing, Y. (**2016**). "Membrane- and plate-type acoustic metamaterials," The Journal of the Acoustical Society of America **139**(6), 3240–3250, doi: 10.1121/1.4950751.

Langfeldt, F., and Gleine, W. (**2019**). "Membrane- and plate-type acoustic metamaterials with elastic unit cell edges," Journal of Sound and Vibration **453**, 65–86, doi: 10.1016/j.jsv.2019.04.018.

Langfeldt, F., and Gleine, W. (**2020**). "Optimizing the bandwidth of plate-type acoustic metamaterials," The Journal of the Acoustical Society of America **148**(3), 1304–1314, doi: 10.1121/10.0001925.

Langfeldt, F., Gleine, W., and von Estorff, O. (**2015**). "Analytical model for low-frequency transmission loss calculation of membranes loaded with arbitrarily shaped masses," Journal of Sound and Vibration **349**, 315–329, doi: 10.1016/j.jsv.2015.03.037.

Langfeldt, F., Gleine, W., and von Estorff, O. (**2018**). "An efficient analytical model for baffled, multi-celled membrane-type acoustic metamaterial panels," Journal of Sound and Vibration **417**, 359–375, doi: 10.1016/j.jsv.2017.12.018.

Langfeldt, F., Riecken, J., Gleine, W., and von Estorff, O. (**2016**). "A membrane-type acoustic metamaterial with adjustable acoustic properties," Journal of Sound and Vibration **373**, 1–18, doi: 10.1016/j.jsv.2016.03.025.

Lu, Z., Yu, X., Lau, S.-k., Khoo, B. C., and Cui, F. (**2020**). "Membrane-type acoustic metamaterial with eccentric masses for broadband sound isolation," Applied Acoustics **157**, 107003, doi: 10.1016/j.apacoust.2019.107003.

Naify, C. J., Chang, C.-M., McKnight, G., and Nutt, S. (**2010**). "Transmission loss and dynamic response of membrane-type locally resonant acoustic metamaterials," Journal of Applied Physics **108**(11), 114905, doi: 10.1063/1.3514082.

Naify, C. J., Chang, C.-M., McKnight, G., and Nutt, S. (**2011**a). "Transmission loss of membrane-type acoustic metamaterials with coaxial ring masses," Journal of Applied Physics **110**(12), 124903, doi: 10.1063/1.3665213.

Naify, C. J., Chang, C.-M., McKnight, G., and Nutt, S. R. (**2012**). "Scaling of membrane-type locally resonant acoustic metamaterial arrays," The Journal of the Acoustical Society of America **132**(4), 2784–92, doi: 10.1121/1.4744941.

Naify, C. J., Chang, C.-M., McKnight, G., Scheulen, F., and Nutt, S. (**2011**b). "Membrane-type metamaterials: Transmission loss of multi-celled arrays," Journal of Applied Physics **109**(10), 104902, doi: 10.1063/1.3583656.

Popa, B.-I., and Cummer, S. A. (**2014**). "Non-reciprocal and highly nonlinear active acoustic metamaterials," Nature Communications **5**, 3398, doi: 10.1038/ncomms4398.

Popa, B.-I., Shinde, D., Konneker, A., and Cummer, S. A. (**2015**). "Active acoustic metamaterials reconfigurable in real time," Physical Review B **91**(22), 220303, doi: 10.1103/PhysRevB.91.220303.

Rohlfing, J., Gardonio, P., and Elliott, S. J. (**2011**). "Base impedance of velocity feedback control units with proof-mass electrodynamic actuators," Journal of Sound and Vibration

330(20), 4661–4675, doi: 10.1016/j.jsv.2011.04.028.

Singleton, L., Cheer, J., and Daley, S. (**2022**). “A robust optimised shunted electrodynamic metamaterial for multi-mode vibration control,” Journal of Sound and Vibration **527**, 116861, doi: 10.1016/j.jsv.2022.116861.

Tan, J., Cheer, J., and Daley, S. (**2022**). “Realisation of nonreciprocal transmission and absorption using wave-based active noise control,” JASA Express Letters **2**(5), 054801, doi: 10.1121/10.0010454.

Xiao, S., Ma, G., Li, Y., Yang, Z., and Sheng, P. (**2015**). “Active control of membrane-type acoustic metamaterial by electric field,” Applied Physics Letters **106**, 091904, doi: 10.1063/1.4913999.

Xiao, S., Tang, S. T., and Yang, Z. (**2017**). “Voltage-tunable acoustic metasheet with highly asymmetric surfaces,” Applied Physics Letters **111**(19), 194101, doi: 10.1063/1.5005603.

Yang, M., Li, Y., Meng, C., Fu, C., Mei, J., Yang, Z., and Sheng, P. (**2015**). “Sound absorption by subwavelength membrane structures: A geometric perspective,” Comptes Rendus Mécanique **343**(12), 635–644, doi: 10.1016/j.crme.2015.06.008.

Yang, M., Ma, G., Wu, Y., Yang, Z., and Sheng, P. (**2014**). “Homogenization scheme for acoustic metamaterials,” Physical Review B **89**(6), 064309, doi: 10.1103/PhysRevB.89.064309.

Yang, Z., Dai, H. M., Chan, N. H., Ma, G. C., and Sheng, P. (**2010**). “Acoustic metamaterial panels for sound attenuation in the 50–1000 Hz regime,” Applied Physics Letters **96**(4), 041906, doi: 10.1063/1.3299007.

Yang, Z., Mei, J., Yang, M., Chan, N. H., and Sheng, P. (**2008**). "Membrane-type acoustic metamaterial with negative dynamic mass," Physical Review Letters **101**(20), 204301, doi: 10.1103/PhysRevLett.101.204301.

Zhang, Y., Wen, J., Zhao, H., Yu, D., Cai, L., and Wen, X. (**2013**). "Sound insulation property of membrane-type acoustic metamaterials carrying different masses at adjacent cells," Journal of Applied Physics **114**(6), 063515, doi: 10.1063/1.4818435.

Zhou, G., Wu, J. H., Lu, K., Tian, X., Huang, W., and Zhu, K. (**2020**). "Broadband low-frequency membrane-type acoustic metamaterials with multi-state anti-resonances," Applied Acoustics **159**, 107078, doi: 10.1016/j.apacoust.2019.107078.